I and Qs Simulation and Processing Envisaged for Spaceborne Polarization Diversity Doppler Radars

Original

I and Qs Simulation and Processing Envisaged for Spaceborne Polarization Diversity Doppler Radars / Battaglia, Alessandro; Rizik, Ali; Sikaneta, Ishuwa; Tridon, Frederic. - In: IEEE TRANSACTIONS ON GEOSCIENCE AND REMOTE SENSING. - ISSN 0196-2892. - 63:(2025), pp. 1-14. [10.1109/tgrs.2025.3529672]

Publisher:
Institute of Electrical and Electronics Engineers Inc.

Published
DOI:10.1109/tgrs.2025.3529672

I and Qs simulation and processing envisaged for space-borne polarisation Diversity Doppler Radars

Alessandro Battaglia, Ali Rizik, Ishuwa Sikaneta, Frederic Tridon

***Abstract*—**

The WIVERN (WInd VElocity Radar Nephoscope) mission concept, a candidate for ESA's Earth Explorer 11 program, aims at globally observing vertical profiles of reflectivity and line-of-sight winds in cloudy and precipitating regions. WIVERN employs a 94 GHz dual-polarisation Doppler radar with conical scanning to address the limited coherence duration between radar transmitted from low-Earth satellites with small antennas. This system transmits closely spaced pairs of horizontally and vertically polarised pulses, which are better correlated than pulses of the same polarization separated by longer intervals. The Polarisation Diversity Pulse Pair (PDPP) technique is then used to estimate radar observables like reflectivities, differential reflectivities, Doppler velocities, and differential phase.

The paper introduces an efficient method for generating H- and V-I&Q time series from the covariance matrix of the autocorrelation function. This method treats the signal as a non-stationary stochastic process, making it suitable for the PDPP pulse sequence from a rapidly rotating antenna and more computationally efficient than inverse fast Fourier transform techniques. It also accounts for interfering cross-polar signals and decorrelation from the scanning antenna. This method is included in the mission's end-to-end simulator, which processes data from raw I&Q to Level 1 estimates of polarimetric variables.

For scientific applications, averaging at least 5 km (40 polarisation diversity pairs) is necessary to reduce noise in polarimetric variables and Doppler velocities. Under optimal conditions, uncertainties at 5 km integration are 0.7 dB for reflectivities, 0.3 dB for Z_{DR}, 0.4 m/s for Doppler velocities, and 1.9° for Φ_{DP}.

***Index Terms*—Doppler radar, winds, polarisation diversity, I&Q simulation, reflectivity differential ratio, differential phase shift.**

I. INTRODUCTION

WIVERN, short for WInd VElocity Radar Nephoscope (www.wivern.polito.it, [1], [2]), was proposed in 2020 to the ESA's Earth Explorer 11 call with the specific aim of filling the observational gap of global winds inside storms and precipitation systems [3]. WIVERN, selected as one of the two best candidate missions, is currently in Phase A with a final decision expected in July 2025. If selected, the satellite will be launched in 2032.

WIVERN's observing principle is based on the well-established Doppler radar theory, with samples collected by a 94 GHz conically scanning antenna rotating at high speed (one full rotation in 5 s). WIVERN's unique 94 GHz conically scanning Doppler radar would provide the first space-based in-cloud profile of line of sight wind, joint with cloud and precipitation profile measurements. The assimilation of line-of-sight (LoS) in-cloud wind profiles over an 800 km swath (providing near-global, quasi-daily, kilometer-scale coverage) is expected to significantly improve numerical weather prediction ([3]). WIVERN would help address fundamental scientific questions about clouds, climate, and atmospheric dynamics. For instance, it would enable, for the first time, space-based observations of atmospheric dynamics within tropical cyclones [4], while also filling existing gaps in polar precipitation observations [3], [5].

As part of ESA's Phase A study, an end-to-end simulator for the mission is being developed to simulate from level 0 (raw measurements) to level 2 (cloud and wind products) and to test instrument performance. Of particular interest is the characterization of the errors on the winds and on the polarimetric variables that WIVERN will be able to observe for the first time from space: differential reflectivity (Z_{DR}), differential phase (Φ_{DP}) and cross-correlation (ρ_{HV}).

This paper aims to present an efficient technique for simulating Level 0 measurements (i.e. the complex voltages measured by the radar receiver from the different ranges) for synthetic scenes generated with cloud-resolving models such as those presented in [2]. Then, the performance of the Doppler velocity and polarimetric variable estimators is evaluated as a function of signal-to-noise ratio and integration distance.

Sect. II briefly reviews the WIVERN polarisation diversity pulse scheme, while Sect. III explains how to simulate Doppler spectra and polarimetric variables. The technique for simulating the I&Q signal is described in detail in Sect. IV, and the estimators of the various variables are discussed in Sect. V. Finally, the results are presented in Sect. VI and conclusions are drawn in Sect. VII.

II. WIVERN PULSE SCHEME

To map horizontal winds, WIVERN will use a W-band radar with a fast, large conically scanning antenna at an angle of incidence of 42° (see specifications in Tab. I e Fig. 1). Measuring Doppler velocities from fast-moving platforms such as satellites in low Earth orbit with good accuracy is quite challenging [6], [7]. WIVERN adopts the Polarisation Diversity (PD) Pulse Pair (PDPP) technique [8], which uses alternating

---

A. Battaglia is with the Department of Physics and Astronomy, University of Leicester, Leicester, UK; NCEO, Leicester, UK and DIATI, Politecnico di Torino, Turin, Italy (e-mail: ab474@leicester.ac.uk, alessandro.battaglia@polito.it).

A. Rizik, F. Tridon, are with the Department of Environment, Land and Infrastructure Engineering, Politecnico di Torino, Turin, Italy (e-mail: {ali.rizik, frederic.tridon.

Ishuwa Sikaneta is with the European Space Agency (ESA), ESTEC, Noordwijk, Netherlands (e-mail: ishuwa.sikaneta@esa.int).

Manuscript received Month DD, YYYY; revised Month DD, YYYY.

TABLE I
WIVERN ORBIT AND RADAR SPECIFICS AS CURRENTLY ESTABLISHED IN PHASE-A OF THE ESA EARTH EXPLORER 11 PROGRAM.

Spacecraft height, H_{SC}	500 km
Spacecraft velocity, v_{SC}	7600 ms^{-1}
Orbit inclination, i	97.42°
Orbit Local Time of the ascending node, $LTAN$	06:00
Incidence scanning angle	42°
Swath width at ground	800 km
Radar transmitted frequency,	94.05 GHz
Radar wavelength,λ	3.2 mm
Antenna angular velocity, Ω_a	12 rpm
Antenna 3-dB beamwidth (azimuth× elevation)	$0.072° \times 0.066°$
Footprint speed	500 kms^{-1}
Single pulse minimum detectable reflectivity	-18 dBZ
polarisation diversity pulse separation, T_{HV}	20 μs
Pair repetition frequency, PRF	4 kHz
Nyquist velocity, V_{Nyq}	40 m/s
Unambiguous range, r_{max}	37.5 km

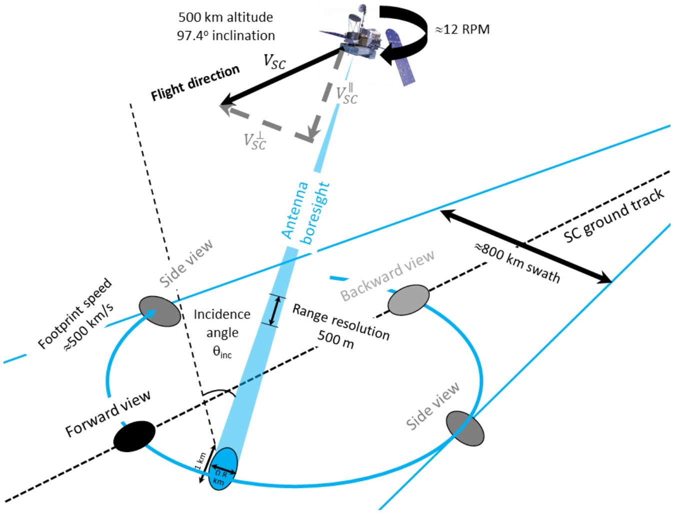

Fig. 1. Conical scan of the WIVERN radar: as the antenna scans a full rotation the satellite advances approximately 35 km at the ground.

pulse pair transmission between H-V (H-leading, V-trailing) and V-H (V-leading, H-trailing) pairs (see Fig. 2, [8], [9]). A polarization diversity radar system uses two channels to simultaneously receive the scattered power of pulses with orthogonal polarisations to measure the first two Doppler moments. These pulses are closely spaced, with a pulse-pair separation denoted T_{HV}, and transmitted in pairs with a pair separation equal to T_p. Despite the use of separate receiver channels for the horizontal (H) and vertical (V) pulses, their strong phase coherence, resulting from the short interval between their transmissions, is of paramount importance in extracting the Doppler velocity. In short, the PD technique effectively decouples the maximum unambiguous range

$$r_{max} = \frac{cT_p}{2} \tag{1}$$

from the Nyquist velocity

$$V_{Nyq} = \frac{\lambda}{4T_{HV}} \tag{2}$$

where c is the speed of light and λ is the radar wavelength, thereby successfully resolving the Doppler dilemma.

III. SIMULATION OF DOPPLER SPECTRA AND POLARIMETRIC VARIABLES

There is a strong heritage in the simulation of hydrometeor Doppler spectra at 94 GHz ([12], [13]) for vertically pointing ground-based non-moving radars. Under such conditions, the spectral power spread is mainly induced by the different terminal velocities of the hydrometeor with an additional spectral broadening induced by air turbulence and by the wind shear across the radar backscattering volume (see right panel in Fig. 3). For a slant-looking radar, the spectral separation due to the different hydrometeor fall velocities is partially attenuated by the cosine of the angle of incidence [14]. At 94 GHz, the presence of non-Rayleigh scattering for typical millimeter-sized meteorological targets such as raindrops leads to non-Gaussian spectra with the presence of secondary peaks and so-called Mie notches [10] (black lines, left panel of Fig. 3).

In contrast, for fast-moving radars, the width of the Doppler spectra is dominated by the broadening effect due to the different directions of the satellite speed along the different directions within the antenna beamwidth. This spectral width generally dominates and renders the spectra Gaussian-like (red-filled spectra in the left panel of Fig. 3). The presence of non-uniform beam filling effects can distort the Gaussian behavior [15] as illustrated in the bottom inset, left panel of Fig. 3.

In the case of WIVERN, this Doppler fading is approximately equal to $\sigma_D \approx \frac{v_{SC}^{\perp}\theta_{3dB}}{4\sqrt{\log(2)}}$ [11], [16], [17], $v_{SC}^{\perp}$ being the spacecraft velocity perpendicular to the antenna boresight (see Fig. 1). When using the parameters of Tab. I this formula produces an apparent wind shear with velocities ranging between ± 2.0 m s^{-1} and $\pm$ 2.9 m s^{-1} across the 3 dB footprint depending on the azimuthal scanning angle of the radar antenna with broader spectra at side views (see Fig. 1) where $v_{SC} = v_{SC}^{\perp}$. Thus, in the first approximation, the Doppler spectra measured by WIVERN can be assumed to be Gaussian with a fixed spectrum width σ_D. Doppler broadening due to dispersion of falling particle velocities is usually less than 1 m/s, thus negligible. The same applies to turbulence broadening, except for very turbulent environments.Realistic co-polar Doppler spectra in the horizontal polarisation $\mathcal{S}_{HH}$ are therefore generated from target spectral reflectivity $\mathcal{Z}_{m,HH}$

$$\mathcal{S}_{HH}(r,\, v) = \frac{\mathcal{C}|K_w|^2}{r^2}\mathcal{Z}_{m,HH}(r,\, v), \tag{3}$$

with r the range, v the Doppler velocity bin, $\mathcal{C}$ the radar constant [18] and $|K_w|^2$=0.75 the dielectric factor for liquid water at 10°C and 94 GHz [19]. In the specific case of Gaussian spectra everything can be expressed in terms of the reflectivity $Z_{m,HH}$ and the mean Doppler velocity v_D according to:

$$\mathcal{S}_{HH}(r,v) = \frac{\mathcal{C}|K_w|^2}{r^2}\frac{Z_{m,HH}(r)}{\sqrt{2\pi}\sigma_D}\exp\left[-\frac{(v - v_D(r))^2}{2\sigma_D^2}\right]. \tag{4}$$

Knowing the spectral differential reflectivity $\mathcal{Z}_{DR}(r, v)$ of atmospheric targets at range r, the co-polar Doppler spectrum

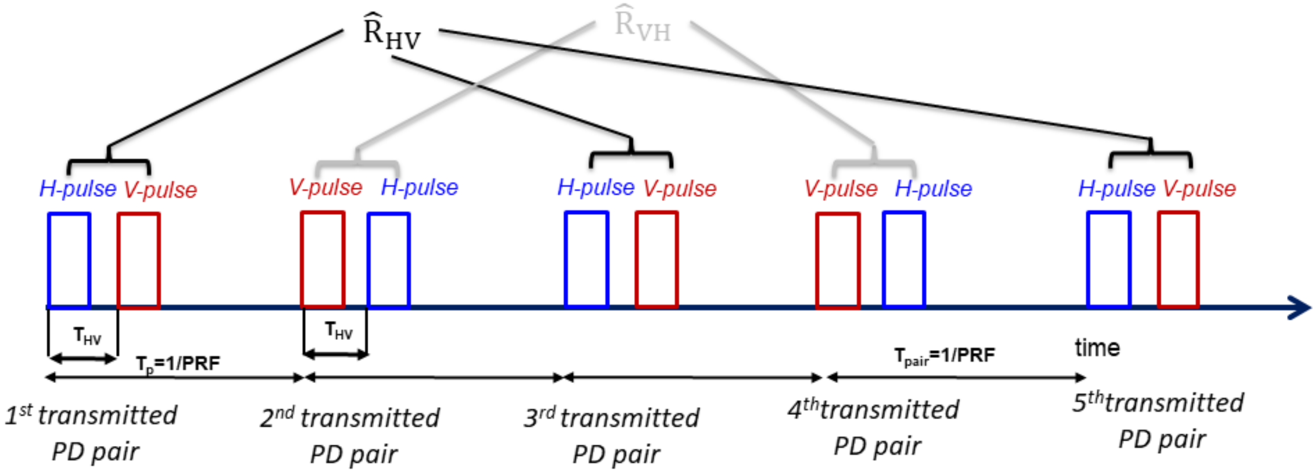

Fig. 2. Pulse patterns of polarisation diversity (PD). The terms H and V denote polarisations in the H and V directions, respectively; while T_{HV} and T_p represent a pulse-pair interval and a pair repetition interval, respectively. This example shows three $H-V$ and two $V-H$ PD pairs.

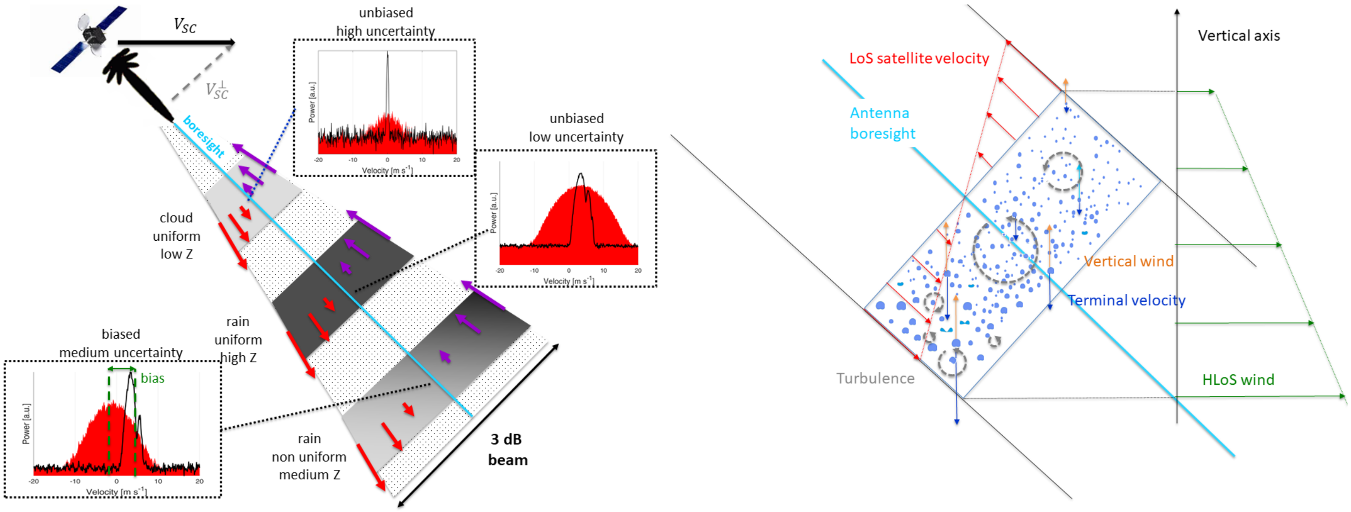

Fig. 3. Left panel: schematic representation for the effects shaping the Doppler spectra in slant-looking spaceborne radars (here the radar is assumed to be forward-looking). Three radar sampling volumes are highlighted corresponding to 1) a low reflecting cloud uniformly distributed over the volume; 2) a uniform rain layer; 3) a rain layer with Z decreasing towards the ground (e.g. due to evaporation). The color shading of the backscattering volumes indicates the strength of the Z signal. The vertical arrows indicate the apparent velocity introduced to the volume due to the motion of the satellite (violet toward and red away from the satellite); note that the velocity of the satellite along the antenna boresight $v_{SC}^{\parallel}$ can be easily subtracted out. Black curves: Doppler spectra that would be observed by a motionless platform (note the characteristic Mie notches in the rain spectra, [10]). Red areas: Doppler spectra broadened by the satellite motion. Note the introduction of biases in the presence of non-uniform beam filling [11]. Right panel: different mechanisms causing spectral broadening: turbulence, vertical and horizontal line of sight (HLoS) wind shear, and variability of terminal velocities within the backscattering volume (similar to ground-based radar observations) plus satellite Doppler fading (unique to low-Earth-orbiting radar observations).

of hydrometeors in the vertical polarisation $\mathcal{S}_{VV}$ can be derived from $\mathcal{S}_{HH}$:

$$\mathcal{S}_{VV}(r,v) = \mathcal{S}_{HH}(r,v)/\mathcal{Z}_{DR}(r,v) \tag{5}$$

Similarly, from the spectral linear depolarisation ratio $\mathcal{LDR}(r,v)$ of atmospheric targets at range r, cross-polar Doppler spectra of hydrometeors $\mathcal{S}_{HV}$ and $\mathcal{S}_{VH}$ are derived from the co-polar Doppler spectra according to:

$$\begin{aligned} \mathcal{S}_{HV}(r,v) &= \mathcal{S}_{HH}(r,v)\ \mathcal{LDR}(r,v) \\ \mathcal{S}_{VH}(r,v) &= \mathcal{S}_{VV}(r,v)\ \mathcal{LDR}(r,v) \end{aligned} \tag{6}$$

where the first and second subscripts represent transmission and reception respectively. Note that, in first approximation $\mathcal{Z}_{\mathcal{DR}}$ and $\mathcal{LDR}$ can be assumed to be uniformly distributed over the velocity interval (then the quantity will be indicated as $Z_{DR}(r)$ and $LDR(r)$), though fully spectral polarimetric modeling is available (e.g. [14], [20]). This is particularly true at the W-band where, because of the scattering resonances, $\mathcal{Z}_{\mathcal{DR}}$ is only changing from between -0.5 to 0.5 dB for raindrops with sizes up to 6 mm and has even smaller variability for snow and graupel particles. For $\mathcal{LDR}$, the spectral variability can be much larger but with very large values occurring in correspondence with small particles that do not contribute much to the overall signal [21].

The in-phase (I) and quadrature (Q) simulation is initiated based on the available knowledge of the Doppler spectrum.

The forward model generates ideal Doppler spectra for the receiving channels, denoted as H and V. In the context of polarization diversity, because of the possible interference between the H- and V-polarised pulses [22], it becomes essential to consider both the co- and the cross-polar components in the Doppler and reflectivity profiles. For the $j-th$ pair (indicated with $[j]$), the total power spectral densities in H and V channels are given by:

$$\begin{aligned}\mathcal{S}_{H}^{[j]}(r,v) &= \mathcal{S}_{HH}^{[j]}(r,v) + \mathcal{S}_{VH}^{[j]}(r-\Delta r_{T_{HV}},v) + \mathcal{N}_{H}^{[j]}(r,v)\\ \mathcal{S}_{V}^{[j]}(r,v) &= \mathcal{S}_{VV}^{[j]}(r,v) + \mathcal{S}_{HV}^{[j]}(r+\Delta r_{T_{HV}},v) + \mathcal{N}_{V}^{[j]}(r,v)\end{aligned} \tag{7}$$

where $S_{VH} = S_{HV}$, S_{HH}, S_{VV} represent the cross-polar and the co-polar power spectral densities, respectively and $\mathcal{N}_H$, and $\mathcal{N}_V$ are the spectral noise power at the output of the H and V polarized receivers, respectively, at a given range r. The cross-polar component originates leakages into the cross-polar receiver (hereafter referred to as “ghost” effects) at ranges shifted either upward or downward by $\Delta r_{T_{HV}} = cT_{HV}/2$, i.e. the range associated with the time between the dual polarisation pair as described in [9], [22]. In addition to the co- and cross-polar spectra at each range the specification of the propagation differential phase coefficient K_{DP}, of the cross-correlation and the differential phase shift at backscattering is needed to generate the I&Q data of the WIVERN system.

IV. SIMULATION OF I & Q TIME SERIES

In previous studies [9], [17] simulations of I&Q for PDPP radars have used the classical method proposed by [23] and successfully applied to simulate the raw signal for the EarthCARE radar [24]–[26]. In that approach, the Doppler spectra, sampled within the Nyquist interval with enough points to capture the spectral variability, are subjected to the inverse discrete Fourier transform technique to extract an in-phase (I) and quadrature-phase (Q) voltage time series.

This method is tailored for a sequence of radar pulses that are equally spaced and where the same spectrum can be representative of a multitude of pulses (i.e. when the process is quasi-stationary), as for EarthCARE. In the case of WIVERN, the sequence of H- and V-polarised pulses is not transmitted with constant time separation: each polarisation diversity pair is separated by a short interval T_{HV} (of the order of 20 μs) and is transmitted alternating the order of the two orthogonal polarisation states (H and V) with a pair repetition time of T_p (of the order of 250 μs, see Fig. 2).

Because of the fast-rotating antenna, the illuminated volumes change significantly from pair to pair (while the effect is negligible for the two pulses of the same pair), so the process cannot be considered stationary across different pairs. The IFFT method can be applied to PDPP but at the cost of generating a large number of I&Q for each pair of pulses. For example, if the spectrum is sampled at a resolution of 0.2 m/s over a Nyquist interval of the order of 40 m/s, approximately 400 I&Q are generated, but only one pair is downselected in the worst-case scenario that the Doppler spectrum changes for successive H-V pairs; otherwise, if the spectrum can be considered stationary for a long integration time (in this case $400 \times 20\ \mu s = 8\ ms$) then the number of I&Q must be undersampled by a factor equal to $1/(PRF \times T_{HV}) \approx 12$. This is very inefficient. For PDPP, the approach proposed by [27], [28] 1) is significantly more computationally efficient. For instance, assuming stationarity, this method achieves at least an 8.25-fold improvement in speed compared to the IFFT-based approach, 2) relies only on the specification of the correlation properties between pulses (hence it works also in non-stationary conditions), and 3) can handle sequences of arbitrarily separated pulses.

In the following, each Doppler velocity spectrum can be converted into the frequency domain via:

$$\mathcal{S}^{[j]}(r,f) = \frac{\lambda}{2}\mathcal{S}^{[j]}(r,v); \qquad f = \frac{2v}{\lambda} \tag{8}$$

where f is the frequency Doppler shift at backscattering and λ is the radar-transmitted wavelength. It is worth noting that the convention of positive velocity toward the radar is adopted here.

A. Covariance matrix of the signal

The correlation between the different pulses in the transmitted sequence can be characterized by the different power spectral density $\mathcal{S}_{xy}^{[j]}(f,\ r)$, where x and y are equal H or V and $[j]$ indicates a pair index. The autocorrelation function at lag τ is defined as:

$$R_{xy}^{[j]}(\tau,r) = \int_{-\infty}^{+\infty} \mathcal{S}_{xy}^{[j]}(f,r)\exp(\imath\, 2\,\pi\, f\, \tau)\, df \tag{9}$$

where $\imath = \sqrt{-1}$.

Note that the correlation at lag-0 $R_{xy}^{[j]}(0,r)$ corresponds to the total power $P_{xy}^{[j]}(r)$ (P_{HH} is the co-polar power for H-pol radiation, P_{VV} is the co-polar power for V-pol radiation and $P_{HV} = P_{VH}$ is the cross-polar power). Note that in the computation of the integral, it is important to keep a spectral resolution δf to resolve the spectrum so that $\delta f\ \tau \ll 1$ (or in the velocity domain $\delta v \ll \lambda/(2\tau)$). For typical Doppler widths for the WIVERN radar (between 2 and 5 m/s) all correlation functions can be considered negligible for $\tau > 500\,\mu$s.

Similarly the cross-correlation between different spectra at lag τ can be modeled as:

$$\begin{aligned}C_{x\ y}^{[j,l]}(\tau,r) = \rho_{vol}(j,l)\int_{-\infty}^{+\infty} \rho_{pol}(x,y)\sqrt{\mathcal{S}_{xx}^{[j]}(f,r)\mathcal{S}_{yy}^{[l]}(f,r)}\\ \exp(\imath\, 2\,\pi\, f\, \tau)\, df\end{aligned} \tag{10}$$

where ρ_{vol} describes the loss of correlation due to the loss of volume overlap caused by the rapidly rotating antenna (see Fig. 4), ρ_{pol} is equal to 1 if $x = y$, otherwise $\rho_{pol}(h,v) = \rho_{HV}(0)e^{-i\,\Psi_{dp}}$ is the loss of correlation between different polarisations at lag-0, where $\Psi_{dp} = \Phi_{dp} + \delta_{dp}$ corresponds to a differential phase shift introduced as a result of a differential shift in propagation (Φ_{dp}) and in backscattering (δ_{dp}) and ρ_t the decorrelation introduced by the time difference between the pulses.

The term $\rho_{pol}(x,\ y)$ is spectral dependent because both the correlation coefficient at lag-0 ($\rho_{HV}(0)$) and δ_{dp} depend on the dimension of the scatterers (though this variability is weak and limited to some resonance sizes, [14]), thus via the

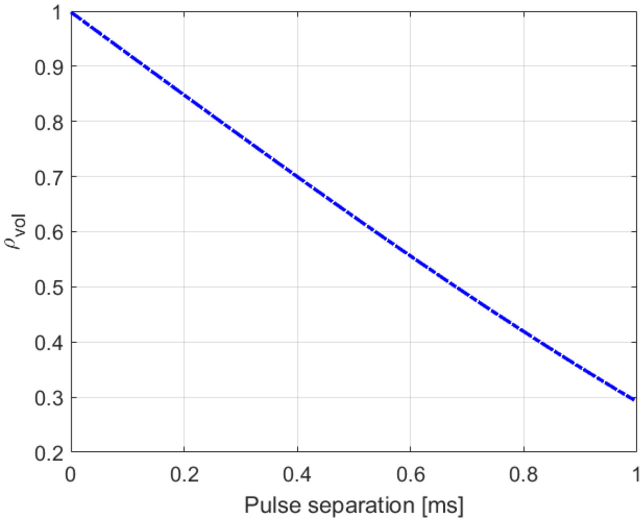

Fig. 4. Decorrelation between two pulses due to the decrease in volume overlap associated with the antenna rotation as a function of pulse separation.

size-terminal velocity relationship they introduce a spectral dependence. This is why ρ_{pol} is kept inside the integral.

In the case of Gaussian Doppler velocity spectra (with mean velocity v_0 and spectral width σ_v), stationary conditions (i.e. the spectra are the same for all pulses) and no spectral dependence of the polarimetric variables, then

$$C_{x\,y}^{[j,l]}(\tau,r) = \rho_{vol}(j,l)\rho_{pol}(x,y)\underbrace{e^{-\frac{8\pi^2\sigma_v^2\tau^2}{\lambda^2}}e^{-\frac{\imath\,4\pi v_0\tau}{\lambda}}}_{\rho_t(\tau)} \qquad (11)$$
$$\sqrt{P_{xx}^{[j]}(r)P_{yy}^{[l]}(r)}$$

where we have introduced $\rho_t(\tau)$, the decorrelation between Gaussian Doppler spectra at time τ, as in [8].

It is important to underline that our formulation does not require neither the Gaussianity nor the stationarity assumption. Eqs. (9-10) in fact can be applied in any condition. In particular, the non-stationarity is automatically accounted for when computing Eqs. (10). This peculiar feature represents a strong advantage of the proposed methodology.

A time series of the complex voltage components corresponding to a sequence of M pairs of pulses can be represented by a complex $2M$ vector $\mathbf{V} = \mathbf{I} + \imath\mathbf{Q}$. The voltages behave like normally distributed with zero mean [18], so their covariances completely determine their behavior. The covariances between the elements of the vector $\mathbf{V}$ can be represented by a $2M \times 2M$ complex matrix $\langle \mathbf{V} \otimes \mathbf{V} \rangle$ (the brackets denote an ensemble mean, $\otimes$ the dyadic product) given in Eq. 12,

where $\star$ denotes conjugation and where we have dropped the r dependence in the terms in the matrix. Here it is assumed that, for any given pulse of a given H-V pair, only the pulses in the two H-V pairs immediately before and after it have a non-negligible correlation. In fact, even with a narrow Gaussian spectral width of 2 m/s at 94 GHz the decorrelation in Eq. (11) already drops to 0.11 and 1.5×10^{-4} after 250 and 500 μs, respectively.

In reality, if only simulations of level 1 PDPP processing are required, it is necessary to simulate the correct correlations only between PD pulses in the same pair, so the correlation matrix can be written as a block matrix with only 2×2 blocks in the diagonal other than zero (i.e. the bold terms in the matrix). In this situation, each polarisation diversity pair is uncorrelated with all other pairs and therefore can be generated independently of all others (see Appendix A).

B. Covariance matrix of the ghosts

In the PDPP approach, ghost interference enters through the response from scatterers at ranges different than the target range. These ranges are separated from the target range in time by $\pm T_{HV}$ according to whether the V pulse follows the H pulse or vice-versa [9]. Cross-polarized ghost interference is uncorrelated to any other signal received at the same apparent range, therefore the ghost covariance matrix becomes a diagonal matrix:

While there is no correlation for the ghosts received at range r in the H-channel and the ghosts received at the same range in the V-channel there is an excellent correlation between the ghosts signals separated in range by $2\Delta r_{T_{HV}}$ because in that case $|\rho_{pol}| = 1$ with the other decorrelation terms having similar expressions to those discussed in Eq. (10). This could be used to recover the Doppler if a surface region provides ghosts with powers dominating the total signals in both channels as demonstrated in Fig. 5, where the term $\hat{G}_{HV}(r, T_{HV})$ represents the correlation function between the ghost signal received from the V channel at the H channel and the copolar signal at the H channel. Conversely, $\hat{G}_{VH}(r, T_{HV})$ corresponds to the correlation function under the opposite scenario.

This may be the case for (land) surfaces, whose cross-signal is generally high (owing to the high cross-polarized normalised radar cross section of the surface, σ_0^{vh}) with the surface ghosts dominating the signal above and below the surface in the two receivers. On the other hand, it is more unlikely to happen for atmospheric targets that usually have very low LDRs.

C. Covariance matrix of the noise

Additive white noise contributes to the overall covariance with a term given by

$$\mathcal{R}_N(r) = P_N\,\mathbb{I}_{2M}$$

where $\mathbb{I}_{2M}$ is the $2M \times 2M$ identity matrix, and P_N is expected to be -15 dBZ noise equivalent power for WIVERN [3]. If the noise levels are different in the two receivers (H and V) then the matrix will be diagonal with $P_{N,V}$ or $P_{N,H}$ depending on which channel is used in reception.

D. Generation of complex I&Q time series

Once a cloud scene and an illumination corresponding to M successive pairs have been specified, a sequence of M vv and hh Doppler spectra can be computed at any given range r, accounting for the different illuminated volumes.

$$\langle \mathbf{V} \otimes \mathbf{V} \rangle \equiv \mathcal{R}_{\mathbf{S}}(\mathbf{r}) = \begin{pmatrix} R^{[1]}_{HH}(0,r) & C^{[1,1]}_{HV}(T_{HV},r) & C^{[1,2]}_{HV}(T_p,r) & C^{[1,2]}_{HH}(T_p+T_{HV},r) & C^{[1,3]}_{HH}(2T_p,r) & C^{[1,3]}_{HV}(2T_p+T_{HV},r) & \cdots \\ C^{\star[1,1]}_{HV}(T_{HV},r) & R^{[1]}_{VV}(0,r) & C^{[1,2]}_{VV}(T_p-T_{HV},r) & C^{[1,2]}_{VH}(T_p,r) & C^{[1,3]}_{VH}(2T_p-T_{HV},r) & C^{[1,3]}_{V,V}(2T_p,r) & \cdots \\ C^{\star[1,2]}_{HV}(T_p,r) & C^{\star[1,2]}_{VV}(T_p-T_{HV},r) & R^{[2]}_{VV}(0,r) & C^{[2,2]}_{VH}(T_{HV},r) & C^{[2,3]}_{VH}(T_p,r) & C^{[2,3]}_{VV}(T_p+T_{HV},r) & \cdots \\ C^{\star[1,2]}_{HH}(T_p+T_{HV},r) & C^{\star[1,2]}_{VH}(T_p,r) & C^{\star[2,2]}_{VH}(T_{HV},r) & R^{[2,2]}_{HH}(0,r) & C^{[2,3]}_{HH}(T_p-T_{HV},r) & C^{[2,3]}_{HV}(T_p,r) & \cdots \\ \vdots & \vdots & \vdots & \vdots & \vdots & \vdots & \vdots \end{pmatrix} \tag{12}$$

$$\mathcal{R}_G(r) = \begin{pmatrix} R^{[1]}_{HV}(0,r-\Delta r_{T_{HV}}) & 0 & 0 & 0 & 0 & 0 & \cdots \\ 0 & R^{[1]}_{VH}(0,r+\Delta r_{T_{HV}}) & 0 & 0 & 0 & 0 & \cdots \\ 0 & 0 & R^{[2]}_{VH}(0,r-\Delta r_{T_{HV}}) & 0 & 0 & 0 & \cdots \\ 0 & 0 & 0 & R^{[2]}_{HV}(0,r+\Delta r_{T_{HV}}) & 0 & 0 & \cdots \\ \vdots & \vdots & \vdots & \vdots & \vdots & \vdots & \vdots \end{pmatrix}. \tag{13}$$

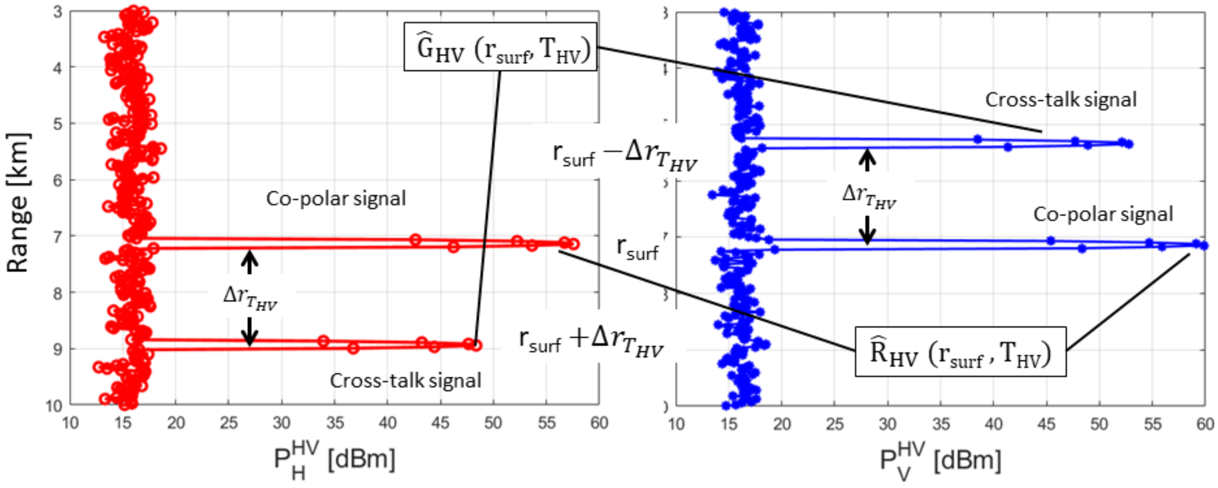

Fig. 5. Diagram illustrating the possibility of correlating the cross-talk signals from the surface to infer the surface Doppler velocity.

The correlation matrix expressed in Eq. (12) can be computed from these spectra at each range. Similarly the sequence of M cross-pol hv Doppler spectra can be computed at range $r - \Delta r_{T_{HV}}$ and $r + \Delta r_{T_{HV}}$ so that $\mathcal{R}_G(r)$ follows from Eq. (13).

Finally, the total covariance matrix can be written as:

$$\mathcal{R}_T(r) = \mathcal{R}_S(r) + \mathcal{R}_G(r) + \mathcal{R}_N(r) \tag{14}$$

where $\mathcal{R}_S$ is the matrix of the signal due to the different polarization effects, $\mathcal{R}_G$ is the matrix of the ghost signals, and $\mathcal{R}_N$ is the matrix of the noise. The procedure is repeated for each single range bin as illustrated in Fig. 6. Note that $\mathcal{R}_T(r)$ at any given range r is the sum of three contributions: 1) $\mathcal{R}_S(r)$ which results from the 2M Doppler spectra (M for VV and M for HH) at range r; 2) $\mathcal{R}_S(r)$ which is affected by the M cross-polar spectra at ranges $r - \Delta r_{T_{HV}}$ and $r + \Delta r_{T_{HV}}$; 3) $\mathcal{R}_N$ which is range independent and is affected by the noise levels of the two receivers. To generate complex voltages which are stochastic variables correlated by the matrix R a technique already proposed to simulate EarthCARE Doppler signal [27], [28] is implemented. Because $\mathcal{R}_T$ is Hermitian and positive definite, it may be written as $\mathcal{R}_T = T^\dagger T$ via Cholesky decomposition, where † denotes Hermitian transpose. Given $2M$ zero-mean independent standard circular Gaussian random variables, y_1, y_2, $\ldots y_{2M}$ [i.e. $y_j = 1/\sqrt{2}(\xi_j + \imath\, \eta_j)$ where ξ_j and η_j are normally distributed with mean equal 0 and standard deviation equal 1]

$$\mathbf{V} = \begin{bmatrix} I_H^{[1]} + \imath Q_H^{[1]} \\ I_V^{[1]} + \imath Q_V^{[1]} \\ I_V^{[2]} + \imath Q_V^{[2]} \\ I_H^{[2]} + \imath Q_H^{[2]} \\ \vdots \\ I_H^{[M]} + \imath Q_H^{[M]} \\ I_V^{[M]} + \imath Q_V^{[M]} \end{bmatrix} = \mathbf{T}^\dagger \begin{bmatrix} y_1 \\ y_2 \\ y_3 \\ y_4 \\ \vdots \\ y_{2M-1} \\ y_{2M} \end{bmatrix} \tag{15}$$

have components distributed as normally distributed variables with zero mean and with correlation provided by $\mathcal{R}_T$.
I&Q components are generally over-sampled in range, i.e. they are sampled with separation in a range smaller than the actual radar range resolution. In WIVERN the range resolution is 500 m, with an expected oversampling by a factor of 3 or 5. This introduces a correlation in the range between voltages received at different range gates [28]. This correlation can be accounted for either by building a correlation matrix similar to Eq. (14) or, more simply like done in [24], by convolving the

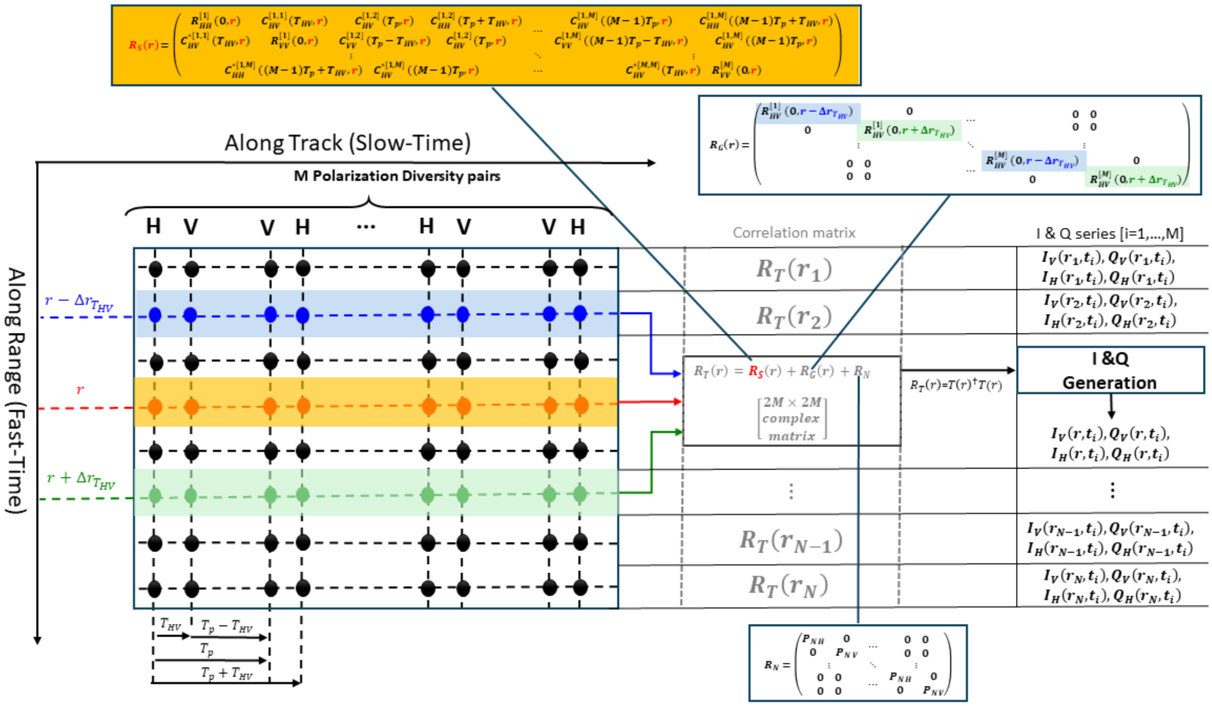

Fig. 6. Schematic for the generation of $\mathcal{R}_T$ and I&Qs. For M PD-pairs at each range bin, a matrix $2M \times 2M$ is built based on the autocorrelation and cross-correlation of the 2M spectra (Eqs. (9-11) at the given range r (red color) and on the cross polar leakages at ranges $r - \Delta r_{T_{HV}}$ (blue color) and $r + \Delta r_{T_{HV}}$ (green color). From the $2M \times 2M$ correlation matrix at each range a sequence of M I&Q for the H channel and M I&Q for the V channel is generated via Eq. (15).

IQs generated at the finest resolution with the radar weighting function, e.g. of the form:

$$W(r-r_0) = C \begin{cases} 1 - \frac{|r-r_0|}{\Delta r} + \frac{1-\alpha}{2\pi\alpha} \sin\left(\frac{2\pi|r-r_0|}{\Delta r}\right) & \text{if } |r-r_0| \leq \Delta r \\ 0 & \text{if } |r-r_0| > \Delta r \end{cases} \quad (16)$$

where $\Delta r = c\tau_p/2$ is the range resolution for a square pulse of length τ_p and C is a normalization constant. The weighting function is characteristic of each radar and results from the combined effect of the finite receiver response time (represented here by a Hamming filter, α being equal to 0.54), and the finite length of the radar pulse.

V. PDPP ESTIMATORS

A. Power estimators

For the H-V pairs the received mean power, $\hat{P}_H^{HV}$ and $\hat{P}_V^{HV}$, received in the H and V channel respectively are estimated as:

$$\hat{P}_H^{HV}(r) = \frac{2}{M} \sum_{k=1}^{M/2} V_H^{[2k-1]*}(r)\, V_H^{[2k-1]}(r)$$
$$\hat{P}_V^{HV}(r) = \frac{2}{M} \sum_{k=1}^{M/2} V_V^{[2k-1]*}(r)\, V_V^{[2k-1]}(r) \quad (17)$$

where M is the number of pulse pairs used for averaging. A similar expression holds for the V-H pairs. The radar reflectivity factor can be deduced from the noise-subtracted power using the following formula:

$$\hat{Z}_x^{HV,VH}(r) = \frac{(\hat{P}_x^{HV,VH}(r) - \hat{P}_N)r^2}{\mathcal{C}|K_{\mathrm{w}}|^2} \qquad x = H,\ V \quad (18)$$

where $\hat{P}_N$ is an estimate of the noise power.

The differential reflectivity, Z_{DR}, is estimated as the ratio between the reflectivities in the H and V channels:

$$\hat{Z}_{DR}^{HV,VH}(r) = \frac{\hat{Z}_H^{HV,VH}(r)}{\hat{Z}_V^{HV,VH}(r)} \quad (19)$$

B. Doppler velocity and Φ_{DP} estimators

The PDPP technique estimates the Doppler velocity via the cross-correlation function of signals with orthogonal polarisations at lag $\tau = T_{HV}$. Mathematically, such correlation functions can be estimated from the voltages of Eq. (15) by the equation ([8], [29]):

$$\hat{R}_{HV}(r, T_{HV}) = \frac{2}{M} \sum_{k=1}^{M/2} V_H^{[2k-1]*}(r)\, V_V^{[2k-1]}(r)$$
$$\hat{R}_{VH}(r, T_{HV}) = \frac{2}{M} \sum_{k=1}^{M/2} V_H^{[2k]}(r)\, V_V^{[2k]*}(r) \quad (20)$$

where $\hat{R}_{HV}$ and $\hat{R}_{VH}$ are the cross-correlation estimated from $M/2$ the H-V and V-H pulse pairs, respectively. From Eqs. (20) [8] proposed to estimate the velocity as:

$$\hat{v}_D = -\frac{\lambda}{4\pi T_{HV}} \arg \sqrt{\hat{R}_{HV}(r,T_{HV})\, \hat{R}_{VH}(r,T_{HV})}$$
$$= -\frac{\lambda}{8\pi T_{HV}} \arg \left(\hat{R}_{HV}(r,T_{HV})\, \hat{R}_{VH}(r,T_{HV})\right) \quad (21)$$

which has the advantage that the bias introduced by any propagation or backscattering differential phase shift is automatically canceled out but reduces the ambiguous velocity interval to $\pm\frac{\lambda}{8T_{HV}}$, as opposed to the standard $\pm\frac{\lambda}{4T_{HV}}$. However, an approach that recovers the complete unambiguous Nyquist interval was presented by [18], [30]. This approach requires first the estimate of ϕ_{DP} as:

$$\hat{\phi}_{DP} = \frac{1}{2}\arg\left(\hat{R}_{HV}(r,T_{HV})\hat{R}^{\star}_{VH}(r,T_{HV})\right) \quad (22)$$

so that the Doppler velocity estimator becomes:

$$\hat{v}_D = -\frac{\lambda}{4\pi T_{HV}}\arg\left(\hat{R}_{HV}(r,T_{HV})\, e^{-\imath\,\hat{\phi}_{DP}}\right) \quad (23)$$

which gives exactly the same result as Eq. (21), apart from the folding. Both estimators presented in Eqs. (21) and Eq. (23) exhibit identical noise characteristics because they are based on averaging the same number of samples ($M/2$). Therefore the estimator (23) is superior because it recovers the full Nyquist interval.

Velocities that fall outside the $\pm V_{Nyq}$ interval (spectrum aliasing), are automatically aliased back into the $\pm V_{Nyq}$ interval so that the actual Doppler velocities can be unfolded by simply adding an integer number of $\pm V_{Nyq}$:

$$\hat{v}_D^{dealiased} = \hat{v}_D \pm 2n\, V_{Nyq} \quad (24)$$

For WIVERN (in the exceptional situation of folding) the selection of n is straightforward because V_{Nyq} is very large (40 m/s) and wind uncertainties are generally much lower than such values.

C. ρ_{HV} estimators

Measuring correlation at lag-0 is unattainable through Wivern measurements but the correlation at lag-T_{HV}, which is useful for quality control purposes, can be estimated as:

$$\hat{\rho}_{HV}(T_{HV}) = \frac{|\hat{R}_{HV}(r,T_{HV})|}{\sqrt{\hat{P}_H^{HV}(r)\hat{P}_V^{HV}(r)}} \quad (25)$$

for the H-V pair and with a similar expression for $\hat{\rho}_{VH}(T_{HV})$ for the V-H pair. Previous research by [31] has demonstrated that the ρ_{HV} estimator is prone to bias, particularly in areas with low correlation values and a limited number of averaging samples.

D. Ghost Doppler processing

Following the discussion at the end of Sect. IV-B, it may be useful to introduce also a specific estimator:

$$\begin{aligned}\hat{G}_{HV}(r,T_{HV}) &= \frac{2}{M}\sum_{k=1}^{M/2} V_H^{[2k-1]*}(r+\Delta r_{T_{HV}})\\ &\quad V_V^{[2k-1]}(r-\Delta r_{T_{HV}})\\ \hat{G}_{VH}(r,T_{HV}) &= \frac{2}{M}\sum_{k=1}^{M/2} V_H^{[2k]}(r-\Delta r_{T_{HV}})\\ &\quad V_V^{[2k]*}(r+\Delta r_{T_{HV}})\end{aligned} \quad (26)$$

with the same processing described in Sect. V-B to estimate the Doppler velocity. This methodology could be very useful to recover the Doppler velocity for land surfaces that are characterized by high normalized backscattering cross-sections and high levels of cross-talk (Fig. 5) but have poor correlations between the two co-polar signals and excellent correlations between cross-talk signals (Fig. 7). In that situation, a reduction in SNR associated with the surface linear depolarization ratio could be compensated by improvement in the Doppler estimators associated with the substantial increase in correlation (see results later in Sect. VI-B).

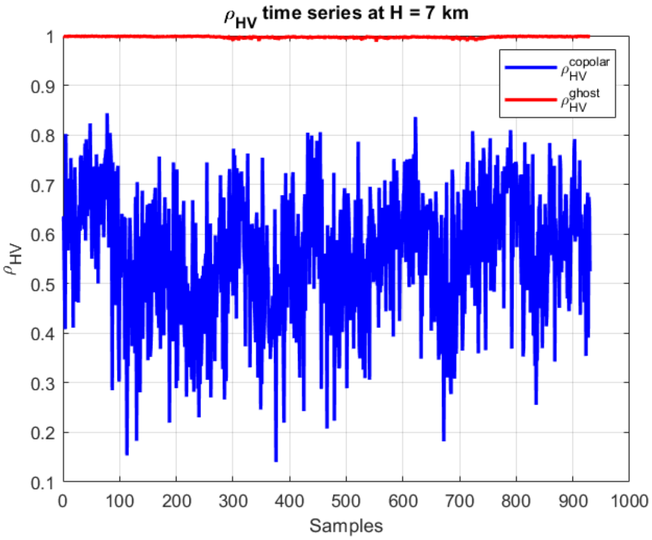

Fig. 7. Correlation between the surface co-polar H- and V-signal from the surface range, r_{surf} (red line) and from the cross-polar H- and V-signal collected at a range $r_{surf} - \Delta r_{T_{HV}}$ and $r_{surf} + \Delta r_{T_{HV}}$ (red line) for a land surface. Data have been collected between Ottawa and Quebec City in Canada for a path between points with lat-lon (46.355,-73.1152) and (46.3438,-73.1450) over land for a total distance of 2.6 km during an airborne field campaign operating a W-band radar in PDPP [32], [33].

WIVERN will have a radiometer mode and will sample at 100 MHz, thus providing a sample every 1.5 m in range. This will ensure an excellent match between the two ranges $r - \Delta r_{T_{HV}}$ and $r + \Delta r_{T_{HV}}$. This operation is only expected to be performed in the on-board processing.

VI. RESULTS

The technique described in the previous sections is first applied to a profile for illustrative purposes and then to assess the performance of the Doppler velocity and polarimetric variable estimators as a function of the signal-to-noise ratio and the integration distance.

A. Example of a vertical profile

A profile that is representative of stratiform rain is used for testing the technique. The profile is derived starting from a CloudSat profile in stratiform rain and making corrections to account for the slant geometry as proposed by [4]. Sensible assumptions for the polarimetric variables are derived from ground-based measurements [22] and are described below. The reflectivity profile has a characteristic increase from the cloud top down to the freezing level located at about 5 km, then it decreases towards the ground due to a combination of rain attenuation and rain evaporation; finally at the surface

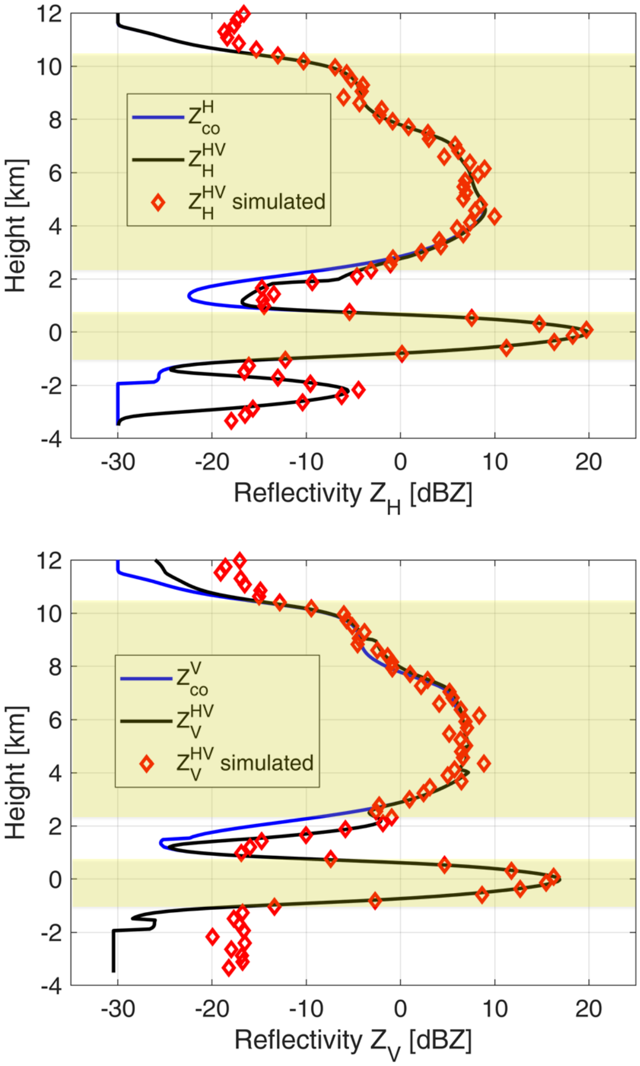

Fig. 8. Reflectivity profile used as a test bed for the I&Q simulation. top (bottom) panel: ideal co-polar reflectivity (red lines) in the H- (V-)channel and ideal received reflectivity (black lines) in the H- (V-)channel for a PDPP H-V pair. The difference between the red and the black lines accounts for the cross-talk interference between the V and the H channels. The red diamonds correspond to the simulated reflectivities expected in the H- (left panel) and the V-channel (right panel). The regions shaded in yellow correspond to ranges where the correlation coefficient at lag T_{HV} exceeds 0.6.

range the reflectivity increases again because of the strong reflecting surface (see red lines in Fig. 8). A variable Z_{DR} is assumed across the whole profile (red line in Fig. 9) with a slight increase in the ice when moving to the melting layer, a peak of 2 dB across the melting, a small value (0.5 dB) in the rain and a 3 dB value for the surface. Similarly, the differential phase shift (black line in the right panel Fig.10) increases steadily from the top of the cloud downward in the ice due to propagation effect (a K_{DP} of the order of 1.2 °/km is assumed) then there is a sharp peak in correspondence to the melting layer (due to phase shift at backscattering on the melting snowflakes) and then decreases very slowly in rain because of slightly negative K_{DP} ([14], [34]).

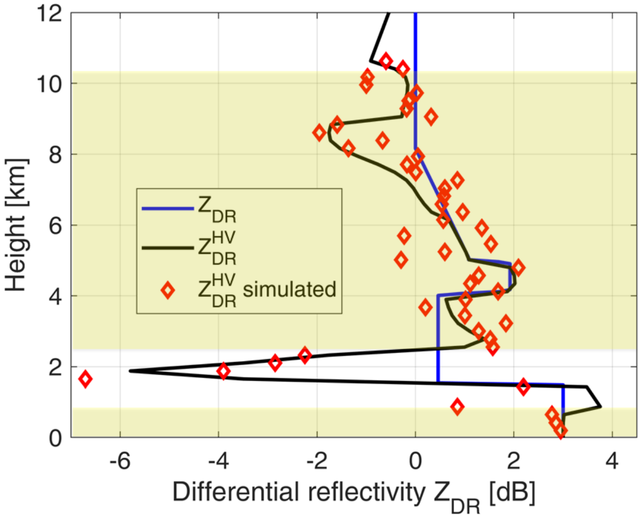

Fig. 9. Differential reflectivity profile used as a test bed for the I&Q simulation with the Z_{DR} computed 1) from the two co-polar reflectivities (red lines), 2) the reflectivities accounting for the ghosts for a PDPP H-V pair (black line), 3) $\hat{Z}_H^{HV}$ and $\hat{Z}_V^{HV}$, the simulated reflectivities after noise subtraction (red diamonds). The regions shaded in yellow correspond to ranges where the correlation coefficient at lag T_{HV} exceeds 0.6.

The wind profile (left panel of Fig. 10), based on CloudSat ECMWF co-located data, shows a peak exceeding 11 m/s at 2.1 km height and then a decrease to few m/s at cloud top. The correlation coefficient at lag 0 (red line in Fig.11) also shows a drop in correspondence to the melting layer (to values smaller than 0.8) but it is assumed high for the other hydrometeor and the surface return (0.98). On the other hand, the correlation at lag T_{HV} that can be computed as

$$\rho_{HV}(T_{HV},r) = \rho_{HV}(0,r)\rho_{vol}(T_{HV})e^{-\frac{8\pi^2\sigma_v^2\tau^2}{\lambda^2}} \sqrt{\frac{P_{HH}(r)\;P_{VV}(r)}{P_H^{HV}(r)\;P_V^{HV}(r)}} \tag{27}$$

drops because of the spectral width (here assumed to be 3 m/s) and the associated decorrelation time (exponential term) but, more importantly, because of the presence of ghosts and noise, both increasing the denominator in the term inside the square root. The ghosts are generated by the linear depolarization ratio, assumed to be -22 dB everywhere apart from the melting layer where a value of -13.5 is assumed.

The simulation framework is applied to this profile. An integration length of 5 km in a horizontal line is assumed. With the WIVERN footprint speed and pair repetition frequency (see Tab. I) this is equivalent to averaging 40 PD pairs (20 H-V and 20 V-H). One realization of the averaged profiles is shown hereafter. As expected the simulated reflectivities, Z_H^{HV} and Z_V^{HV} (Fig. 8, here shown before noise subtraction) are quite noisy even at high SNR because of the limited number of samples but they generally converge to the expected profiles (which include the ghosts generated by the cross-talk). Note the diversity between the H and V channel (top vs bottom panel) because of the difference introduced by the Z_{DR} and

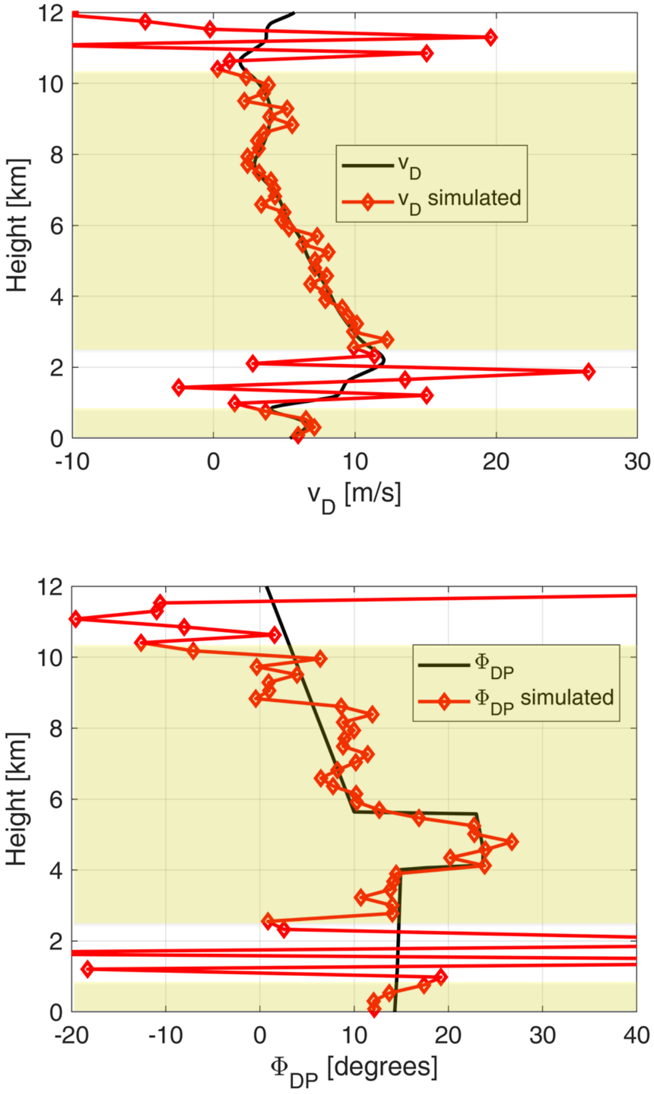

Fig. 10. Doppler velocity (left) and differential phase shift (right) profiles used as a test bed for the I&Q simulation with the ideal profiles in black and the simulated ones with diamonds. The regions shaded in yellow correspond to ranges where the correlation coefficient at lag T_{HV} exceeds 0.6.

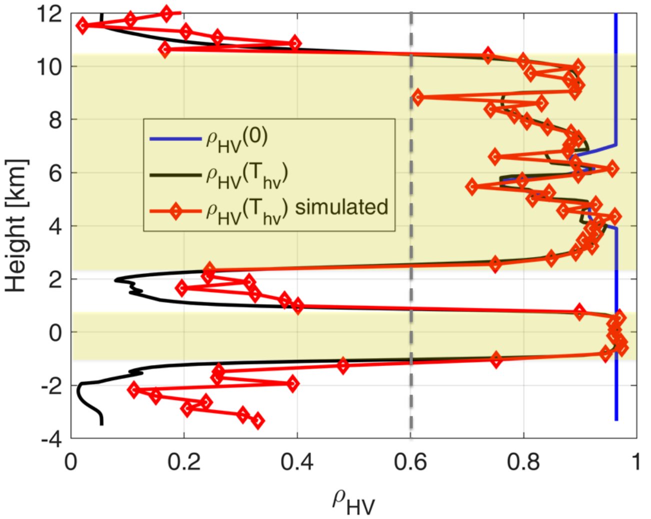

Fig. 11. Correlation coefficient between H and V-polarisations with the ideal profile in black and the simulated ones (which include the effect of ghosts and noise) with diamonds.

by the ghosts. Similarly Z_{DR}^{HV} (Fig. 9) shows errors of the order of 0.5 dB in the region with good SNR. Also note that, because of the presence of the ghosts, the simulated values (red diamonds) do not converge to the intrinsic Z_{DR} (red line) but to Z_{DR}^{HV} (black line) which is affected by ghosts and can take values which are very different from those expected from hydrometeors (e.g. the very negative values at about 2 km height). Therefore, together with ρ_{HV}, this variable can then be used to flag regions affected by ghost contamination.

The Doppler velocities and Φ_{DP} simulated profiles (Fig. 10) show good convergence in the region of high SNR and where the correlation coefficient at lag T_{HV} is larger than 0.6 (regions shaded in yellow). Otherwise, in regions seriously contaminated by random or ghost noise, the Doppler velocities (Φ_{DP} values) tend to be random numbers in the ±40 m/s (±180°) interval. Finally the simulated profile of $\hat{\rho}_{HV}(T_{HV})$ tend to follow the expected value $\rho_{HV}(T_{HV})$ apart from an overestimation when $\rho_{HV}(T_{HV})$ drops below 0.4 (Fig. 11).

B. Errors on polarimetric variable and velocity estimates

An assessment of the errors associated with the reflectivity, Z_{DR}, ϕ_{DP}, Doppler velocity and correlation coefficient estimators provided by Eqs. (18,19,22,23,25), respectively, has been carried out via a Monte Carlo simulation with 40,000 different realizations for different levels of SNR. Errors are established for a (1 km) 5 km along scanning footprint integration, which corresponds to (8) 40 I&Q pairs (20 H-V and 20 V-H). A constant $Z_{DR} = 2$ dB is assumed whereas two values of ρ_{HV} (0.99 and 0.9) are used to illustrate the impact of correlation on the estimates of the different observables.

Reflectivities and Z_{DR} show small positive biases at low SNR (left panels in Fig. 12). The positive bias in Z at small SNR can be explained by the fact that when the noise subtraction is performed realizations where the noise is significantly below the mean noise level are discharged. Results are therefore positively biased. Random errors on Z values on the other hand (right panels) are of the order of 0.6 dB (1.5 dB) at high SNR for 5 km (1 km) integration and rapidly increase respectively to 1.5 dB and 4.5 dB at $SNR = 0$ dB. These errors do not change in a palpable way changing the spectral width and/or the correlation ρ_{HV} at lag 0. For large SNRs, they can be well predicted by the formula:

$$std_{\hat{Z}} = \frac{4.343}{\sqrt{M}}\left(1 + \frac{1}{SNR}\right) \tag{28}$$

as shown by the dashed lines in the top right panel. For Z_{DR} random errors are a strong function of $\rho_{HV}(0)$ (and weakly of σ_v) with smaller correlation producing larger errors (bottom right panel).

Errors in the estimates of mean Doppler velocities (Fig. 13) agree with previous findings ([1], [2], [33]), with the errors

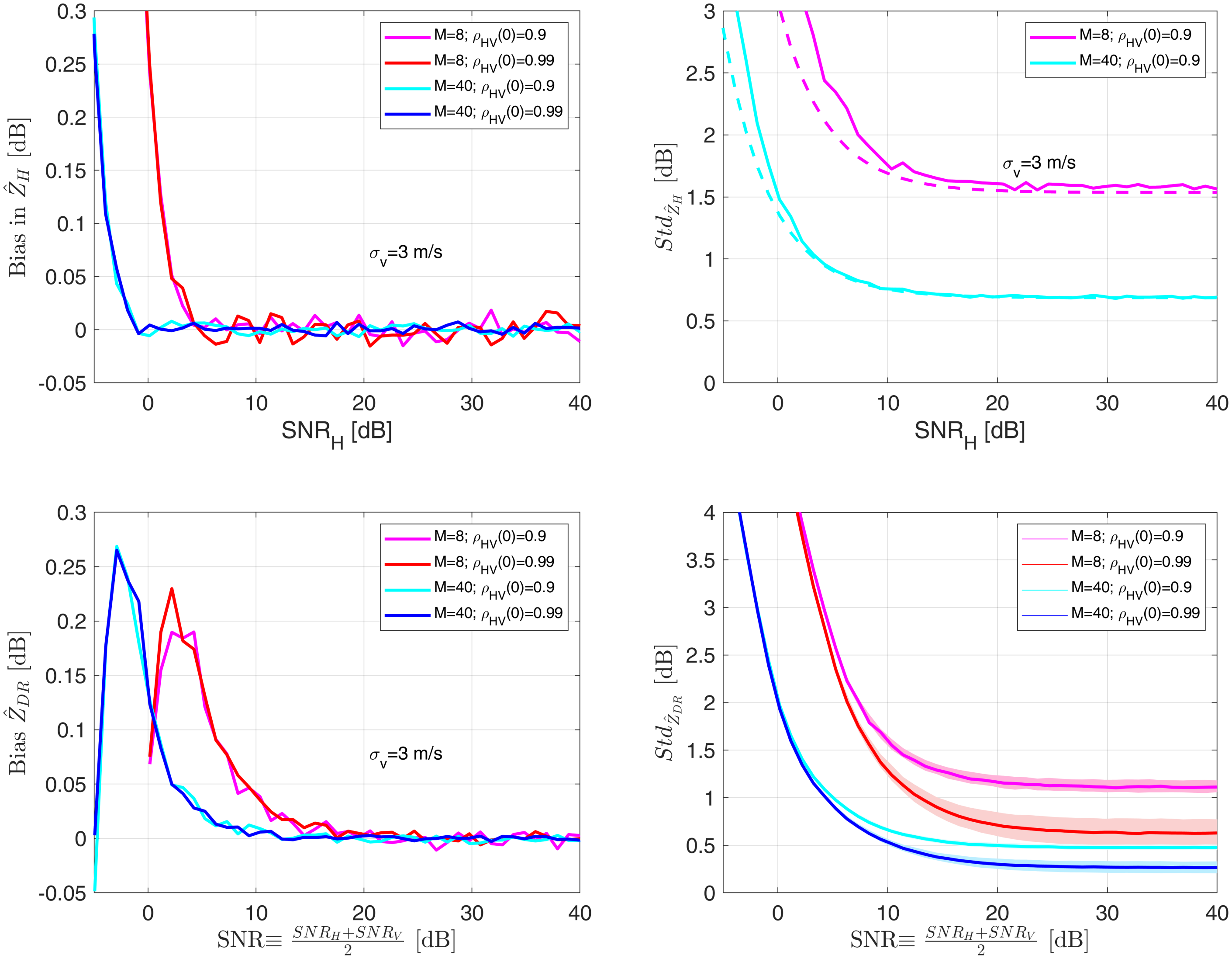

Fig. 12. Bias (left) and standard deviation (right) for the reflectivity, Z_H, and the differential reflectivity, Z_{DR}, estimators in correspondence of an integration of 1 and 5 km (8 and 40 PD pairs, respectively). If present, the shading corresponds to a range of variability in the Doppler spectral widths between 2 and 4 m/s; otherwise a value of 3 m/s is assumed. The dashed lines in the top right panel correspond to the results predicted by Eq. (28).

rapidly decreasing with increasing SNR and plateauing for values larger than 20 dB at 0.40, 0.78, 0.89 and 1.75 m/s (blue, cyan, red and magenta lines , respectively). The errors also show the typical dependence $1/\sqrt{M}$ with the number of integrated pulses. The errors increase drastically when the correlation ρ_{HV} at lag-0 drops, as when in the presence of mixed-phase hydrometeors or ghost echoes ([22]).

The formula proposed by [8]:

$$\text{std}_{\hat{v}_D} = \frac{v_{Nyq}}{2\pi\beta}\sqrt{\frac{1}{2M}\left[\left(1+\frac{1}{\text{SNR}}\right)^2 - \beta^2\right]} \tag{29}$$

where, for Gaussian spectra,

$$\beta \equiv \rho_{HV}(0)\rho_{vol}(T_{HV})\exp\left(-\frac{8\pi^2\sigma_v^2\,T_{HV}^2}{\lambda^2}\right)$$

fits the results of the 5 km integration almost perfectly but underestimates the errors when averaging over a few I&Q with low correlation (compare pink dashed and continuous lines). Formula (29) is valid when perturbation analysis is applicable, i.e. when the following two conditions are satisfied [35]:

$$2\pi\ M\ \frac{\sigma_v}{2v_{Nyq}} >> 1 \tag{30}$$

$$\beta^2\ M \gg \left(1+\frac{1}{\text{SNR}}\right)^2 \tag{31}$$

The first equation, for a characteristic value of $\sigma_v = 3$ m/s reads $M \gg 4$ while the second for $SNR = -6$ dB and $\rho_{HV}(0) = 0.9$ gives $M \gg 33$ which demonstrates that it cannot produce accurate results with $M = 8$ at any SNR and with $M = 40$ for low SNRs. A similar behavior is found for the error in Φ_{DP} (Fig. 14), a direct consequence of the fact that both the errors in the Doppler velocities and in Φ_{DP}

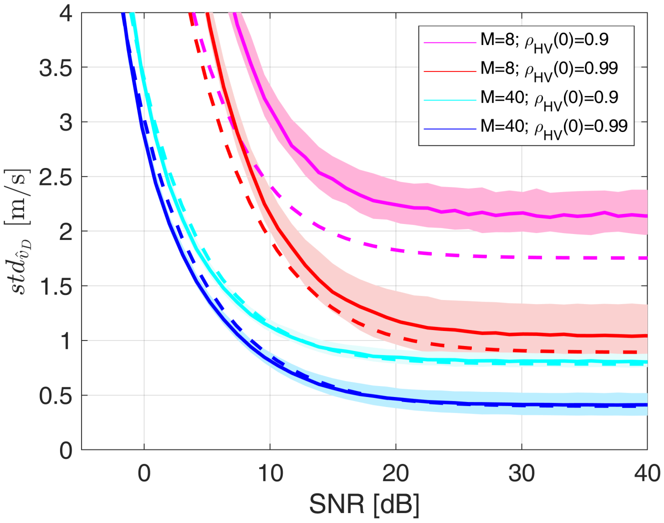

Fig. 13. Standard deviation for the Doppler velocity in correspondence of integration of 1 and 5 km (8 and 40 PD pairs, respectively) and for a spectral width of 3 m/s. The shading corresponds to a range of variability in the Doppler spectral widths between 2 and 4 m/s. The dashed lines correspond to the errors computed according to Eq. 29 for the same configuration as the continuous lines.

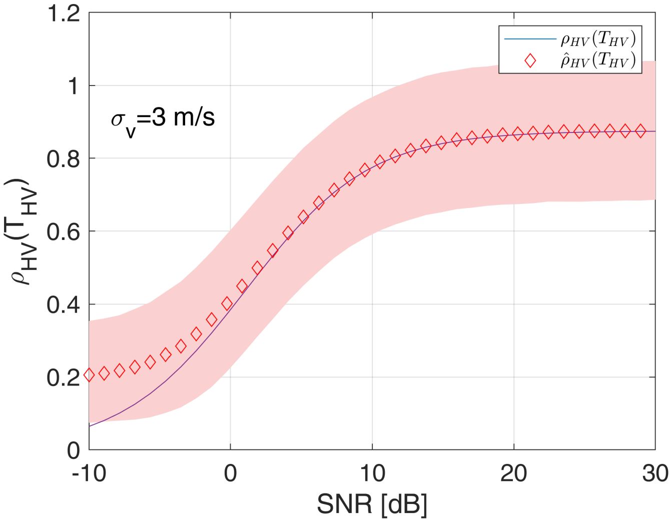

Fig. 15. Behavior of the correlation at lag T_{HV} as a function of SNR for a correlation at lag-0 equal 0.9 (black line).The red diamonds correspond to the mean of the estimator based on Eq. 25 with $M = 40$; the red shaded area identifies the 10th and 90th percentile of the estimates.

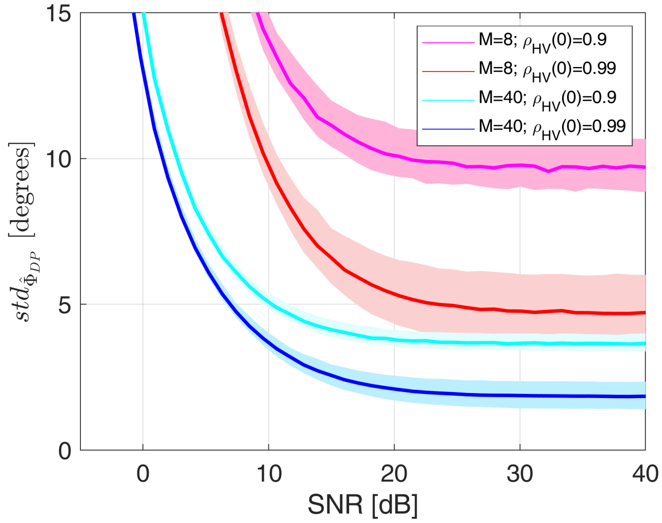

Fig. 14. Same as Fig. 13 for the differential phase shift.

are driven by the errors in the phase determination. When averaging over 40 PD pairs, even with high SNR and with excellent correlation, the error in Φ_{DP} remains of the order of 2.5°.

Finally, the estimated correlation at lag T_{HV} estimated based on Eq. 25 is shown in Fig. 15 as a function of SNR, with the correlation decreasing significantly as we move to lower SNR (see Eq. 25). For values of $SNR < 5$ dB, the estimator becomes positively biased; generally, there is a large standard deviation error on all values of SNR. However, estimates of this parameter from the I&Q processing can be used to check the quality of the other estimators. For example, from the 90th percentile envelope (upper contour of the red shaded area in Fig. 15) it can be concluded that an estimated $\rho_{HV}(T_{HV} red)$ of 0.6 and 0.8 is likely to be greater than 0.4 and 0.6, respectively.

VII. CONCLUSIONS

This paper presents an advanced methodology for simulating I&Q time series for PD radars, such as that planned for the European Space Agency (ESA) WIVERN mission, which is one of the two finalists for Earth Explorer 11. The proposed technique demonstrates significantly improved computational efficiency compared to the inverse Fast Fourier Transform (FFT)-based method developed by [23]. Moreover, this new approach effectively deals with the non-stationarity of the power spectrum during transitions between successive PD pairs. It can also account for the decorrelation introduced by antenna rotation. Finally, in addition to the correlation between the pulses of each PD pair (which is directly exploited in the PDPP Doppler estimates), the weaker correlations between nearby PD pairs can also be included.

The I&Q time series can then be processed to estimate the polarimetric and Doppler radar observables (reflectivity, Z_{DR}, ϕ_{DP}, Doppler velocity, and correlation coefficient estimators). The study shows that for the WIVERN mission, it will be necessary to average at least 5 km (i.e. 40 PD pairs) to reduce the noise of the different polarimetric variables and Doppler velocities to be useful for scientific applications. For such integration distance, under optimal conditions (high SNR and high correlation) the reflectivities, Z_{DR}, Doppler velocities and Φ_{DP} will have uncertainties of 0.7 dB, 0.3 dB, 0.4 m/s and 1.9°, respectively. The possibility of increasing the number of independent samples by reducing the time between different pairs of PDs, either by reducing the time between different pairs of PDs (hence the maximum unambiguous range) or by introducing frequency diversity pairs, is currently being investigated.

APPENDIX

A. Analytical solution of I&Q generation for 2×2 correlation matrices

When the correlation between different PD pairs can be neglected (which is the case if PDPP processing is performed) then the matrix in Eq. (12) becomes block diagonal with each PD pair characterized by a correlation matrix of the form:

$$\mathcal{R}_T = \mathcal{R}_P + \mathcal{R}_I + \mathcal{R}_N = \left[\begin{array}{cc} \mathcal{R}_{11} & \mathcal{R}_{12} \\ \mathcal{R}_{12}^{\star} & \mathcal{R}_{22} \end{array} \right]. \tag{32}$$

Since $\mathcal{R}_T$ is Hermitian, it can be decomposed as

$$\begin{aligned} \mathcal{R}_T = & \left[\begin{array}{cc} \cos(\theta) & e^{\imath\delta}\sin(\theta) \\ e^{-\imath\delta}\sin(\theta) & -\cos(\theta) \end{array} \right] \left[\begin{array}{cc} \lambda_1 & 0 \\ 0 & \lambda_2 \end{array} \right] \\ & \left[\begin{array}{cc} \cos(\theta) & e^{\imath\delta}\sin(\theta) \\ e^{-\imath\delta}\sin(\theta) & -\cos(\theta) \end{array} \right] \end{aligned} \tag{33}$$

where

$$\begin{aligned} \lambda_{max} &= \frac{\mathcal{R}_{11} + \mathcal{R}_{22} + \sqrt{4|\mathcal{R}_{12}|^2 + (\mathcal{R}_{11} - \mathcal{R}_{22})^2}}{2} \\ \lambda_{min} &= \frac{\mathcal{R}_{11} + \mathcal{R}_{22} - \sqrt{4|\mathcal{R}_{12}|^2 + (\mathcal{R}_{11} - \mathcal{R}_{22})^2}}{2} \\ e^{\imath\delta} &= \frac{\mathcal{R}_{12}}{|\mathcal{R}_{12}|} \\ \theta &= \arctan\left(\frac{2|\mathcal{R}_{12}|}{\mathcal{R}_{11} - \mathcal{R}_{22}} \right) \end{aligned} \tag{34}$$

with $\lambda_1 = \lambda_{max}$ and $\lambda_2 = \lambda_{min}$ if $|\mathcal{R}_{11}| > |\mathcal{R}_{22}|$ otherwise $\lambda_1 = \lambda_{min}$ and $\lambda_2 = \lambda_{max}$. Note that the last expression should be computed with the arctan2 function to avoid numerical division by zero.

By defining,

$$T = \left[\begin{array}{cc} \sqrt{\lambda_1} & 0 \\ 0 & \sqrt{\lambda_2} \end{array} \right] \left[\begin{array}{cc} \cos(\theta) & e^{\imath\delta}\sin(\theta) \\ e^{-\imath\delta}\sin(\theta) & -\cos(\theta) \end{array} \right]$$

one finds that $\mathcal{R}_T = T^{\dagger} T$, where † denotes Hermitian transpose.

Given two zero-mean independent standard circular Gaussian random variables, y_1 and y_2, the two complex vectors

$$\left[\begin{array}{c} I_H + \imath Q_H \\ I_V + \imath Q_V \end{array} \right] = T^{\dagger} \left[\begin{array}{c} y_1 \\ y_2 \end{array} \right] \tag{35}$$

are distributed as zero mean variables with a correlation matrix provided by $\mathcal{R}_T$.

ACKNOWLEDGMENTS

This research has been supported by the Italian Space Agency (ASI) project "Scientific studies for the Wind Velociy Radar Nephoscope (WIVERN) mission" (Project number: 2023-44-HH.0) and by the European Space Agency under the activity "End-to-End Performance Simulator Activity of the WIVERN Mission" (ESA Contract Number 4000139446/22/NL/SD).

REFERENCES

[1] A. J. Illingworth, A. Battaglia, J. Bradford, M. Forsythe, P. Joe, P. Kollias, K. Lean, M. Lori, J.-F. Mahfouf, S. Melo, R. Midthassel, Y. Munro, J. Nicol, R. Potthast, M. Rennie, T. H. M. Stein, S. Tanelli, F. Tridon, C. J. Walden, and M. Wolde, "WIVERN: A New Satellite Concept to Provide Global In-Cloud Winds, Precipitation, and Cloud Properties," *Bull. Amer. Met. Soc.*, vol. 99, no. 8, pp. 1669–1687, 2018. [Online]. Available: https://doi.org/10.1175/BAMS-D-16-0047.1

[2] A. Battaglia, P. Martire, E. Caubet, L. Phalippou, F. Stesina, P. Kollias, and A. Illingworth, "End to end simulator for the wivern w-band doppler conically scanning spaceborne radar," *Atm. Meas. Tech.*, vol. 2021, pp. 1–31, 2022. [Online]. Available: https://amt.copernicus.org/preprints/amt-2021-342/

[3] E. WIVERN-RfA, "Wivern report for assessment," ESA-EOPSM-WIVE-RP-4375, Tech. Rep., 2023, available at https://eo4society.esa.int/event/earth-explorer-11-user-consultation-meeting/.

[4] F. Tridon, A. Battaglia, A. Rizik, F. E. Scarsi, and A. Illingworth, "Filling the gap of wind observations inside tropical cyclones," *Earth and Space Science*, vol. 10, no. 11, p. e2023EA003099, 2023, e2023EA003099 2023EA003099. [Online]. Available: https://agupubs.onlinelibrary.wiley.com/doi/abs/10.1029/2023EA003099

[5] F. E. Scarsi, A. Battaglia, and M. Maahn, "How to reduce sampling errors in spaceborne cloud radar-based snowfall estimates," *Atm. Meas. Tech. Disc.*, 2024.

[6] A. Battaglia, P. Kollias, R. Dhillon, R. Roy, S. Tanelli, K. Lamer, M. Grecu, M. Lebsock, D. Watters, K. Mroz, G. Heymsfield, L. Li, and K. Furukawa, "Spaceborne cloud and precipitation radars: Status, challenges, and ways forward," *Reviews of Geophysics*, vol. 58, no. 3, p. e2019RG000686, 2020, e2019RG000686 10.1029/2019RG000686. [Online]. Available: https://agupubs.onlinelibrary.wiley.com/doi/abs/10.1029/2019RG000686

[7] P. Kollias, A. Battaglia, K. Lamer, B. P. Treserras, and S. A. Braun, "Mind the gap - part 3: Doppler velocity measurements from space," *Frontiers in Remote Sensing*, vol. 3, 2022. [Online]. Available: https://www.frontiersin.org/article/10.3389/frsen.2022.860284

[8] A. L. Pazmany, J. C. Galloway, J. B. Mead, I. Popstefanija, R. E. McIntosh, and H. W. Bluestein, "Polarization Diversity Pulse-Pair Technique for Millimeter-WaveDoppler Radar Measurements of Severe Storm Features," *J. Atmos. Ocean Technol.*, vol. 16, no. 12, pp. 1900–1911, 1999. [Online]. Available: https://doi.org/10.1175/1520-0426(1999)016⟨1900:PDPPTF⟩2.0.CO;2

[9] A. Battaglia, S. Tanelli, and P. Kollias, "Polarization Diversity for Millimeter Spaceborne Doppler Radars: An Answer for Observing Deep Convection?" *J. Atmos. Ocean Technol.*, vol. 30, no. 12, pp. 2768–2787, 2013. [Online]. Available: https://doi.org/10.1175/JTECH-D-13-00085.1

[10] P. Kollias, B. A. Albrecht, and F. Marks, "Why Mie? Accurate Observations of Vertical Air Velocities and Raindrops Using a Cloud Radar," *Bull. Amer. Met. Soc.*, vol. 83, pp. 1471–1483, 2002, doi: http://dx.doi.org/10.1175/BAMS-83-10-1471.

[11] S. Tanelli, E. Im, S. L. Durden, L. Facheris, and D. Giuli, "The Effects of Nonuniform Beam Filling on Vertical Rainfall Velocity Measurements with a Spaceborne Doppler Radar," *J. Atmos. Ocean Technol.*, vol. 19, no. 7, pp. 1019–1034, 2002. [Online]. Available: https://doi.org/10.1175/1520-0426(2002)019⟨1019:TEONBF⟩2.0.CO;2

[12] P. Kollias, J. Rémillard, E. Luke, and W. Szyrmer, "Cloud radar Doppler spectra in drizzling stratiform clouds: 1. Forward modeling and remote sensing applications," *J. Geophys. Res. Atm.*, vol. 116, no. D13, 2011. [Online]. Available: https://agupubs.onlinelibrary.wiley.com/doi/abs/10.1029/2010JD015237

[13] F. Tridon and A. Battaglia, "Dual-frequency radar Doppler spectral retrieval of rain drop size distributions and entangled dynamics variables," *J. Geophys. Res. Atm.*, vol. 120, no. 11, pp. 5585–5601, 2015. [Online]. Available: https://agupubs.onlinelibrary.wiley.com/doi/abs/10.1002/2014JD023023

[14] I. Tsikoudi, A. Battaglia, C. Unal, and E. Marinou, "Simulations of spectral polarimetric variables measured in rain at w-band," *EGUsphere*, vol. 2025, pp. 1–22, 2025. [Online]. Available: https://egusphere.copernicus.org/preprints/2025/egusphere-2024-3164/

[15] O. O. Sy and S. Tanelli, "Recovering the Elusive Spectral Width From Spaceborne Doppler Profiling Radar Measurements: The "ExpliSyT" Approach," *IEEE Trans. Geosci. Remote Sens.*, vol. 61, pp. 1–23, 2023.

[16] R. Meneghini and L. Liao, "Effective Dielectric Constants of Mixed-Phase Hydrometeors," *J. Atmos. Ocean Technol.*,

vol. 17, pp. 628–640, 2000, doi: http://dx.doi.org/10.1175/1520-0426(2000)017<0628:EDCOMP>2.0.CO;2.

[17] A. Battaglia and P. Kollias, "Error Analysis of a Conceptual Cloud Doppler Stereoradar with Polarization Diversity for Better Understanding Space Applications," *J. Atmos. Ocean Technol.*, vol. 32, no. 7, pp. 1298–1319, 2015. [Online]. Available: https://doi.org/10.1175/JTECH-D-14-00015.1

[18] R. J. Doviak and D. S. Zrnić, *Doppler Radar and Weather Observations*. Academic Press, 1993.

[19] R. Lhermitte, "Attenuation and Scattering of Millimeter Wavelength Radiation by Clouds and Precipitation," *J. Atmos. Ocean Technol.*, vol. 7, no. 3, pp. 464–479, 1990. [Online]. Available: https://doi.org/10.1175/1520-0426(1990)007⟨0464:AASOMW⟩2.0.CO;2

[20] C. Unal and Y. van den Brule, "Exploring mm-wavelength radar capabilities for raindrop size distribution retrieval: Estimating mass-weighted mean diameter from the differential backscatter phase," *J. Atmos. Ocean Technol.*, 2024. [Online]. Available: https://journals.ametsoc.org/view/journals/atot/aop/JTECH-D-23-0094.1/JTECH-D-23-0094.1.xml

[21] K. Mróz, A. Battaglia, S. Kneifel, L. von Terzi, M. Karrer, and D. Ori, "Linking rain into ice microphysics across the melting layer in stratiform rain: a closure study," *Atm. Meas. Tech.*, vol. 14, no. 1, pp. 511–529, 2021. [Online]. Available: https://amt.copernicus.org/articles/14/511/2021/

[22] A. Rizik, A. Battaglia, F. Tridon, F. E. Scarsi, A. Kötsche, H. Kalesse-Los, M. Maahn, and A. Illingworth, "Impact of crosstalk on reflectivity and doppler measurements for the wivern polarization diversity doppler radar," *IEEE Trans. Geosci. Remote Sens.*, vol. 61, pp. 1–14, 2023.

[23] D. S. Zrnic, "Simulation of weatherlike doppler spectra and signal," *J. Appl. Meteorol.*, vol. 14, pp. 619–620, 1975.

[24] P. Kollias, S. Tanelli, A. Battaglia, and A. Tatarevic, "Evaluation of EarthCARE Cloud Profiling Radar Doppler Velocity Measurements in Particle Sedimentation Regimes," *J. Atmos. Ocean Technol.*, vol. 31, no. 2, pp. 366–386, 2014. [Online]. Available: https://doi.org/10.1175/JTECH-D-11-00202.1

[25] O. O. Sy, S. Tanelli, N. Takahashi, Y. Ohno, H. Horie, and P. Kollias, "Simulation of EarthCARE Spaceborne Doppler Radar Products Using Ground-Based and Airborne Data: Effects of Aliasing and Nonuniform Beam-Filling," *IEEE Trans. Geosci. Remote Sens.*, vol. 52, no. 2, pp. 1463–1479, Feb 2014.

[26] O. Sy, S. Tanelli, P. Kollias, and Y. Ohno, "Application of Matched Statistical Filters for EarthCARE Cloud Doppler Products," *IEEE Trans. Geosci. Remote Sens.*, vol. 52, no. 11, pp. 7297–7316, 2014.

[27] N. A. J. Schutgens, "Simulated Doppler Radar Observations of Inhomogeneous Clouds: Application to the EarthCARE Space Mission," *J. Atmos. Ocean Technol.*, vol. 25, no. 9, pp. 1514–1528, 2008, doi: 10.1175/2007JTECHA1026.1.

[28] ——, "Simulating Range Oversampled Doppler Radar Profiles of Inhomogeneous Targets," *J. Atmos. Ocean Technol.*, vol. 25, no. 1, pp. 26–42, 2008, doi: 10.1175/2007JTECHA956.1.

[29] R. J. Doviak and D. Sirmans, "Doppler Radar with Polarization Diversity," *J. Atmos. Sci.*, vol. 30, no. 4, pp. 737–738, 1973. [Online]. Available: https://doi.org/10.1175/1520-0469(1973)030⟨0737:DRWPD⟩2.0.CO;2

[30] M. Sachidananda and D. S. Zrnić, "Efficient processing of alternately polarized radar signals," *J. Atmos. Ocean Technol.*, vol. 6, no. 1, pp. 173 – 181, 1989. [Online]. Available: https://journals.ametsoc.org/view/journals/atot/6/1/1520-0426_1989_006_0173_epoapr_2_0_co_2.xml

[31] R. Touzi, A. Lopes, J. Bruniquel, and P. W. Vachon, "Coherence estimation for sar imagery," *IEEE Trans. Geosci. Remote Sens.*, vol. 37, no. 1, pp. 135–149, 1999.

[32] A. Battaglia, M. Wolde, L. P. D'Adderio, C. Nguyen, F. Fois, A. Illingworth, and R. Midthassel, "Characterization of Surface Radar Cross Sections at W-Band at Moderate Incidence Angles," *IEEE Trans. Geosci. Remote Sens.*, vol. 55, no. 7, pp. 3846–3859, 2017, 10.1109/TGRS.2017.2682423.

[33] M. Wolde, A. Battaglia, C. Nguyen, A. L. Pazmany, and A. Illingworth, "Implementation of polarization diversity pulse-pair technique using airborne w-band radar," *Atm. Meas. Tech.*, vol. 12, no. 1, pp. 253–269, 2019. [Online]. Available: https://www.atmos-meas-tech.net/12/253/2019/

[34] K. Aydin and Y.-M. Lure, "Millimeter wave scattering and propagation in rain: a computational study at 94 and 140 ghz for oblate spheroidal and spherical raindrops," *IEEE Trans. Geosci. Remote Sens.*, vol. 29, no. 4, pp. 593–601, 1991.

[35] R. J. Doviak and D. S. Zrnić, *Doppler Radar and Weather Observations*. Dover, Mineola, NY, 2006, second edition.

Alessandro Battaglia graduated at the University of Padova, Italy, with a thesis in Particle Physics and received the Ph.D. degree in Physics at the University of Ferrara, Italy. He is experienced in microwave remote sensing of clouds and precipitation with a specific interest in space-borne radars. Currently, he has a joint appointment as an Associate Professor in the Department of Physics at the University of Leicester, Leicester, UK, and at DIATI at Politecnico di Torino, Turin, Italy. He has extensive experience in active and passive microwave modeling, he has developed radar forward modeling capable of simulating Doppler spaceborne radars, he has worked on polarisation diversity, and developed retrieval algorithms for multi-frequency observations. He is a member of the NASA Precipitation Measuring Mission Science Team and of the INCUS Team, a member of the ESA MAG of EarthCARE and WIVERN, and an author or co-author of more than 150 peer-reviewed journal papers.

Ali Rizik holds a diverse academic background, culminating in a Ph.D. in Science and Technology for Electronic and Telecommunication Engineering from the Department of Naval, Electrical, Electronic, and Telecommunications Engineering (DITEN) at the University of Genoa, Italy, in 2021. His journey began with a graduation from the Faculty of Science at the Lebanese University in 2016, where he delved into signal, telecom, image, and speech processing through his thesis. His international exposure includes an internship at ULCO University, France, from April to August 2016, which further enriched his academic and professional experience. Currently, he occupies a postdoctoral position at DIATI at the Politecnico di Torino, Turin, Italy, contributing to the WIVERN spaceborne Doppler radar project. His research interests encompass a broad spectrum, with a primary focus on machine learning applications, radar signal processing, radar target identification for security applications, and the application of radars in meteorology. His research interests also include spaceborne remote sensing and atmospheric convection science.

Ishuwa Sikaneta received an M.Sc. degree in math/physics from the University of Guelph, Guelph, ON, Canada, in 1998, and a Ph.D. degree in electrical engineering from the University of Ottawa, Ottawa, ON, in 2004. From 1998 to 2000, he was with the Canada Center for Remote Sensing, Ottawa, where he focused on polarimetric signal processing and data exploitation. Since 2000, he has been with Defense Research and Development Canada, Ottawa, focusing on air and space-based multi-aperture SAR for imaging and moving-target indication (MTI). Between 2015 and 2021 he worked as a Satellite Imagery Analyst with the International Atomic Energy Agency, Vienna, Austria establishing an operational SAR imagery capability for the ISI section of the IAEA. Since 2021, he has worked as a payloads engineer at the European Space Agency (ESA) at the ESTEC location in Noordwijk, the Netherlands. His research interests include monostatic and bistatic SAR signal processing methods for imaging and MTI, constant false-alarm rate moving-target detection and estimation, waveform and antenna diversities, future SAR system development, and microwave techniques applied to atmospheric radar.

Frederic Tridon completed his PhD in radar meteorology in 2011 at the Laboratoire de Météorologie Physique at Blaise Pascal University in Clermont-Ferrand (France). As a PostDoc, he worked successively at the Department of Physics of the University of Leicester (UK), at the Institute of Geophysics and Meteorology of the University of Cologne (Germany), and is now at DIATI at Politecnico di Torino, Turin (Italy). His research focuses on the characterization of the microphysical processes of cloud and precipitation for a better understanding of their role in the earth's radiation budget and water cycle. In particular, he has extensive experience in the retrieval of liquid and solid precipitation properties, combining multiple-frequency radars, from ground-based, airborne, and spaceborne platforms.